Polymer Testing 157 (2026) 109127

Contents lists available at ScienceDirect

Polymer Testing

journal homepage: www.elsevier.com/locate/polytest

Magnetized carbon microsphere and chitosan-functionalized BN hybrid network in stearic acid–epoxy composites for synergistic thermal management and EMI shielding

Jaekyung Lee [a,1], Jaeyeon Kim [a,1], Oju Kwon [a], Subin Lee [b], Pei-Chen Su [c], Jooheon Kim [a,b,*]

[a] School of Chemical Engineering, Chung-Ang University, Seoul, 06974, Republic of Korea
[b] Department of Intelligent Energy and Industry, Graduate School, Chung-Ang University, Seoul, 06974, Republic of Korea
[c] School of Mechanical and Aerospace Engineering, Nanyang Technological University, 50 Nanyang Avenue, 639798, Singapore

ARTICLE INFO

Keywords:
Phase change materials
Thermal conductivity
Shape stability
Heat management
EMI shielding

ABSTRACT

Developing multifunctional materials that simultaneously address thermal and electromagnetic interference (EMI) challenges is essential for next-generation miniaturized electronic systems. In this study, a chemically bonded stearic acid–epoxy phase-change polymer (SAEP) composite was engineered using magnetized carbon microspheres (MCMs) and chitosan-functionalized boron nitride (CBN) to achieve integrated thermal management, EMI shielding, and mechanical reinforcement. The MCMs, comprising a carbon framework embedded with iron oxide nanoparticles, facilitate both thermal conduction and magnetic-loss-driven EMI absorption. CBN provides high intrinsic thermal conductivity while improving interfacial compatibility with the SAEP matrix because of chitosan-assisted functionalization. Owing to the synergistic effects of these fillers, the optimized SAEP/MCM/CBN composite achieved a through-plane thermal conductivity of 5.11 W m^{-1} K^{-1}, demonstrating a twenty-two-fold improvement over pristine SAEP, while maintaining a high latent heat of 90.5 J g^{-1} to ensure effective heat storage and phase-transition stability. The composite also exhibited strong EMI shielding performance, reaching 65.2 dB within the X-band (8.2–12.4 GHz), with absorption as the dominant mechanism, thereby minimizing secondary electromagnetic reflection. Infrared thermal imaging further confirmed rapid heat dissipation, with CPU surface temperatures reduced by more than 25 °C during operation. Mechanical testing revealed significant enhancements in both tensile strength and elongation due to the interconnected hybrid filler framework. Collectively, these results highlight that combining MCMs with functionalized ceramic fillers within a chemically integrated phase-change material matrix enables simultaneous heat dissipation, EMI attenuation, and mechanical durability. The SAEP/MCM/CBN composite, therefore, represents a robust and scalable platform for advancing thermal interface and EMI shielding in high-power electronic systems.

1. Introduction

The rapid advancement of 5G communication technologies, artificial intelligence, and high-performance computing has accelerated the miniaturization and functional integration of modern electronic devices [1,2]. As circuit dimensions shrink and power densities rise, the accumulation of heat within confined architectures poses a critical threat to device stability, efficiency, and service life. In addition, the high-frequency operation of densely integrated systems generates electromagnetic interference (EMI), which disrupts signal integrity and degrades overall performance [3,4]. Addressing these concurrent challenges necessitates the development of multifunctional materials that can effectively manage both thermal and electromagnetic environments in next-generation electronic systems [5,6].

Traditional thermal management strategies, such as metallic heat sinks and fan-assisted cooling, are becoming increasingly inadequate because of the constraints of compact device designs and elevated heat flux. These strategies increase weight and volume while failing to suppress localized temperature rise. Consequently, polymer-based thermal interface materials (TIMs) and composites have gained attention due to their low density, chemical stability, and manufacturing versatility [7]. However, their intrinsically low thermal conductivity, typically below

* Corresponding author. School of Chemical Engineering, Chung-Ang University, Seoul, 06974, Republic of Korea.
E-mail address: jooheonkim@cau.ac.kr (J. Kim).
[1] Equally contributed to this paper.

https://doi.org/10.1016/j.polymertesting.2026.109127
Received 26 November 2025; Received in revised form 20 January 2026; Accepted 24 February 2026
Available online 28 February 2026
0142-9418/© 2026 The Authors. Published by Elsevier Ltd. This is an open access article under the CC BY-NC-ND license (http://creativecommons.org/licenses/by-nc-nd/4.0/).

0.3 W m^{-1} K^{-1}, significantly limits heat dissipation performance [8]. Furthermore, their weak EMI shielding effectiveness (SE), generally below 10 dB, restricts their applicability in multifunctional systems requiring simultaneous thermal and electromagnetic control.

To overcome these limitations, various thermally conductive fillers such as graphene [9], carbon fibers [10], aluminum nitride (AlN) [11,12], and boron nitride (BN) [13,14] have been incorporated into polymers to improve heat transfer. Conductive fillers including Ag [15], Cu [16], and carbon nanotubes (CNTs) [17] have also been used to enhance EMI shielding. However, high conductive filler loadings tend to induce reflection-dominant shielding, resulting in secondary electromagnetic pollution and reliability risks. Therefore, developing polymer composites that exhibit absorption-dominant EMI shielding while maintaining high thermal conductivity remains a critical challenge. Recent research has demonstrated that combining thermally conductive materials with magnetic fillers such as iron oxide (Fe_3O_4) [18], Ni [19], or Co [20] can simultaneously improve heat dissipation and EMI attenuation. Magnetic components generate magnetic losses through mechanisms such as domain wall and eddy current effects, enabling efficient absorption of incident electromagnetic waves. Additionally, when they are incorporated into polymer matrices, their conductive nature supports the formation of thermally favorable pathways.

Phase-change materials (PCMs) offer an effective approach to thermal regulation by storing and releasing latent heat during melting and crystallization [21,22]. Among available PCMs, stearic acid (SA) is promising because of its high latent heat and chemical stability. However, pristine SA exhibits poor compatibility with polymers and suffers from severe leakage during melting. Although physical blending can improve dispersion temporarily, it cannot establish stable interfacial interactions for long-term thermal management. To address these limitations, chemically integrated PCM–polymer systems have been developed. Reactions such as epoxy–acid coupling allow PCM segments to be covalently incorporated into polymer networks, enhancing phase stability and structural integrity. An SA–epoxy polymer (SAEP) obtained through such coupling offers a stable matrix for the fabrication of multifunctional composites.

In this study, a multifunctional composite system was engineered by incorporating magnetized carbon microspheres (MCMs) and chitosan (CS)-functionalized BN (CBN) into the SAEP matrix. The MCMs consist of a carbon framework containing Fe_3O_4 nanoparticles, enhancing both heat conduction and magnetic-loss-based EMI attenuation. The CBN exhibits high intrinsic thermal conductivity, and CS functionalization enhances compatibility with the SAEP matrix by improving interfacial interactions. The combination of these fillers within the chemically bonded SAEP framework establishes interconnected pathways that facilitate efficient heat transfer and promote electromagnetic energy attenuation. Consequently, the SAEP/MCM/CBN composites demonstrate significant improvements in thermal conductivity, EMI SE, and phase stability. These multifunctional characteristics highlight their potential for next-generation electronic systems that require integrated thermal and electromagnetic management.

2. Experimental

2.1. Materials

SA (≥98%), cellulose powder, Fe_3O_4, and CS (medium molecular weight) were purchased from Sigma-Aldrich (St. Louis, MO, USA). Diglycidyl ether of bisphenol-A (DGEBA; epoxy resin; epoxy equivalent weight = 186.8 g·eq^{-1}) was supplied by Kukdo Chemical Co., and Jeffamine D-230 (amine curing agent; 60 g·eq^{-1}, 0.948 g mL^{-1}) was obtained from New Seoul Chemical Co., Korea. Hexagonal BN (h-BN; purity = 99%, average particle size = 12 μm) was supplied by Momentive Performance Materials, Inc. (USA). Hydrochloric acid (HCl; 37%), acetone, and deionized (DI) water were provided by Dae-Jung Chemical and Metal Co., Ltd. (Seoul, Korea). All chemicals were used as received.

2.2. Fabrication of the SAEP matrix

To prepare the SAEP, SA (2 g) and EP (1 g) were first combined and fully melted in an oil bath at 150 °C. Subsequently, D-230 (0.327 g) was introduced into the molten mixture and stirred slowly on a hot plate maintained at the same temperature until a transparent product (i.e., the SAEP) was obtained through an epoxy–acid coupling reaction.

2.3. Preparation of the MCMs

First, 8 g of cellulose was dissolved in 200 g of an aqueous solution containing 4.5 wt% NaOH and 9.5 wt% thiourea, which had been precooled to −8 °C. After dissolution, the mixture was stirred vigorously for 5 min to yield a transparent cellulose solution.

Cellulose microspheres were prepared using a modified sol–thermal gelation method. First, a homogeneous suspension was formed by mixing 300 mL of paraffin oil with 15 mL of Span 80 under continuous stirring at 1000 rpm for 1 h. Next, 50 mL of the cellulose mixture was added dropwise to the suspension at a rate of 1 mL min^{-1}. The resulting solution was stirred for 10 h to promote gelation. Subsequently, 10 wt% HCl was added until the pH reached 7, triggering the formation of regenerated cellulose microspheres. The supernatant paraffin layer was removed, and the settled product was repeatedly washed with water and acetone to eliminate residual paraffin oil, Span 80, and HCl. The purified regenerated cellulose microspheres were designated as CMs.

Thereafter, carbon microspheres were obtained by calcining the CMs under a nitrogen atmosphere in a tube furnace at 500 °C for 3 h. To magnetize the carbon microspheres, Fe_3O_4 nanoparticles and the as-prepared carbon microspheres were mixed at a weight ratio of 1:2 (Fe_3O_4:carbon microspheres) and dispersed in DI water. The suspension was subjected to bath sonication for 1 h, allowing the Fe_3O_4 nanoparticles to effectively penetrate the porous carbon microspheres. After sonication, the product was washed several times with DI water and collected through filtration to remove unbound nanoparticles. The final product was dried in an oven at 60 °C, yielding the MCMs. Based on the Fe_3O_4-to-carbon microsphere weight ratio used during the magnetization process and the removal of excess nanoparticles through repeated washing, the Fe_3O_4 content in the MCM was 30 wt%.

2.4. Preparation of CBN

CS powder (6 g), BN (2 g), and zirconia balls (150 g) were first combined in a planetary ball mill container and processed at 500 rpm for 12 h using a programmable milling system (BML-2, Daihan Scientific, Korea). The resulting powder was subsequently dispersed in DI water, and the pH of the suspension was adjusted to 6.5. To enhance both the dispersion and interfacial interaction between CS and BN, the suspension was then sonicated using a tip-type sonicator (VCX 750, Sonics & Materials Inc., USA) at 250 W for 1 h. Thereafter, the sonicated suspension was repeatedly washed with DI water and vacuum-filtered through a 0.3 μm nylon membrane. This washing–filtration cycle was performed four times to remove unbound CS. The purified material was finally dried in an oven at 60 °C, yielding CBN.

2.5. Fabrication of SAEP/MCM/CBN composites

To fabricate the composites, the MCM and CBN fillers were first dispersed into the SAEP matrix using a planetary paste mixer until a uniform blend was obtained. The resulting mixture was subsequently transferred into a hot-press mold and cured at 150 °C under 10 MPa for 2 h. The MCM:CBN ratios (e.g., 2:1, 1:1, and 1:2) refer to weight ratios (wt/wt).

2.6. Characterization

Details of the characterization procedures are provided in the Supporting Information.

3. Results and discussion

3.1. Fabrication of PCM-based composites and characterization of SAEP matrix

To fabricate the thermally conductive PCM composites, we first synthesized the SAEP matrix and combined it with the functional fillers, as illustrated in Fig. 1. The SAEP matrix was specifically designed to reinforce the intrinsically weak mechanical properties of PCMs and to suppress leakage during phase transitions. Since there is limited compatibility between SA and epoxy resin, direct blending can result in phase separation. To address this issue, SA was first reacted with the EP through an epoxy–acid coupling reaction, yielding a chemically bonded SAEP network with improved stability and uniformity. MCMs were obtained by carbonizing regenerated cellulose microspheres and subsequently introducing Fe_3O_4 nanoparticles through sonication. CBN was prepared by coating BN with CS using a ball-milling process. Finally, the SAEP, MCMs, and CBN were mixed using a planetary paste mixer and hot-pressed to yield the SAEP/MCM/CBN composites.

FT-IR analysis was conducted to verify the successful synthesis of the SAEP matrix, as presented in Fig. 2(a). The pristine epoxy resin exhibited characteristic peaks at 1608 cm^{-1} and 912 cm^{-1}, which correspond to the aromatic C=C stretching of the EP structure and the C–O–C stretching vibration of the epoxy ring, respectively [23]. SA displayed a distinct carbonyl stretching peak at 1702 cm^{-1}, attributed to the C=O group of its carboxylic acid [24]. After the reaction between SA and EP, the intensity of the 1702 cm^{-1} peak decreased significantly, while a new absorption band emerged at 1735 cm^{-1}, corresponding to the ester C=O stretching mode [25]. Additionally, the peak at 912 cm^{-1} decreased, indicating the ring-opening of epoxy groups during the epoxy–acid coupling reaction. These spectral changes confirm that SA was chemically bonded to the epoxy resin through esterification, validating the successful formation of the SAEP matrix.

Differential scanning calorimetry (DSC) analysis was conducted to investigate the changes in thermal behavior following the formation of the SAEP matrix. As shown in Fig. 2(b), pristine SA exhibited a sharp melting endotherm at approximately 72.5 °C, reflecting its crystalline structure. After the epoxy–acid reaction, the resulting SAEP displayed a broadened endothermic region spanning 52.4–71.7 °C, along with a slight decrease in the melting point to around 64.9 °C. This decrease in melting temperature is attributed to the partial consumption of carboxyl groups during esterification [26]. Since these carboxyl groups contribute to intermolecular hydrogen bonding and enhance the thermal stability of SA crystals, their reduction weakens the crystalline packing, resulting in a lower melting point. Moreover, the broadened peak further indicates a disruption of the ordered SA domains and the formation of a chemically bonded SAEP network. Collectively, the decrease and broadening of the melting transition strongly support that SA was successfully grafted onto the epoxy resin through the epoxy–acid coupling reaction, resulting in a thermally stable and covalently cross-linked SAEP phase. This esterification reaction contributes to the formation of a stable polymer network and is closely associated with the observed phase transformation behavior [27].

The cross-sectional morphologies of pure EP, SA, and the synthesized SAEP were examined using FE-SEM (Fig. 2(c–e)). Pure EP exhibited a smooth and dense fracture surface, while SA had a crystalline layered structure. In contrast, the SAEP presented a uniform and continuous morphology without visible crystalline domains, indicating the successful incorporation of SA into the epoxy matrix through esterification. This homogeneous microstructure confirms the improved compatibility between SA and EP and the formation of an integrated SAEP network.

Table 1 summarizes the mechanical performance and latent heat of SAEP matrices prepared using different SA-to-EP ratios. Compared to pure SA, the SAEP system demonstrated a remarkable enhancement in mechanical robustness, with the tensile strength increasing by more than 310% and the strain improving by over 34%. In addition, the SAEP matrix with an SA:EP ratio of 2:1 maintained relatively high latent heat, preserving approximately 70% of the thermal energy storage capacity of pristine SA. These results demonstrate that the SAEP matrix achieves an excellent balance between mechanical reinforcement and thermal storage functionality, underscoring its strong potential as an advanced PCM.

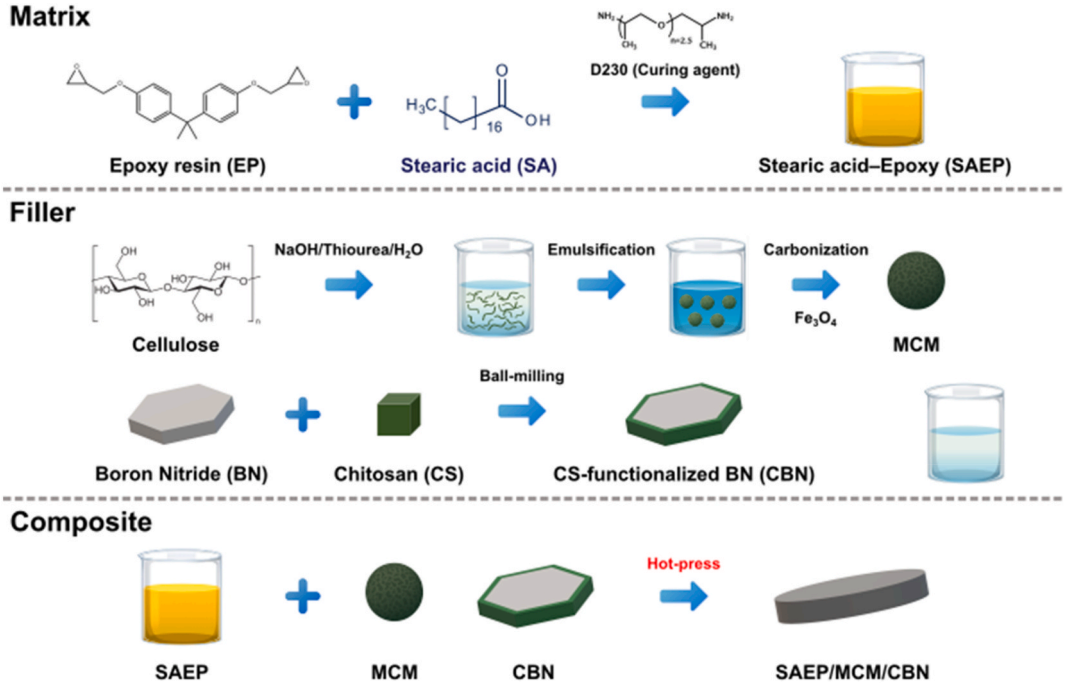


Fig. 1. Schematic illustrating the synthesis of the SAEP matrix, the preparation of MCM and CBN fillers, and the fabrication of the SAEP/MCM/CBN composite.

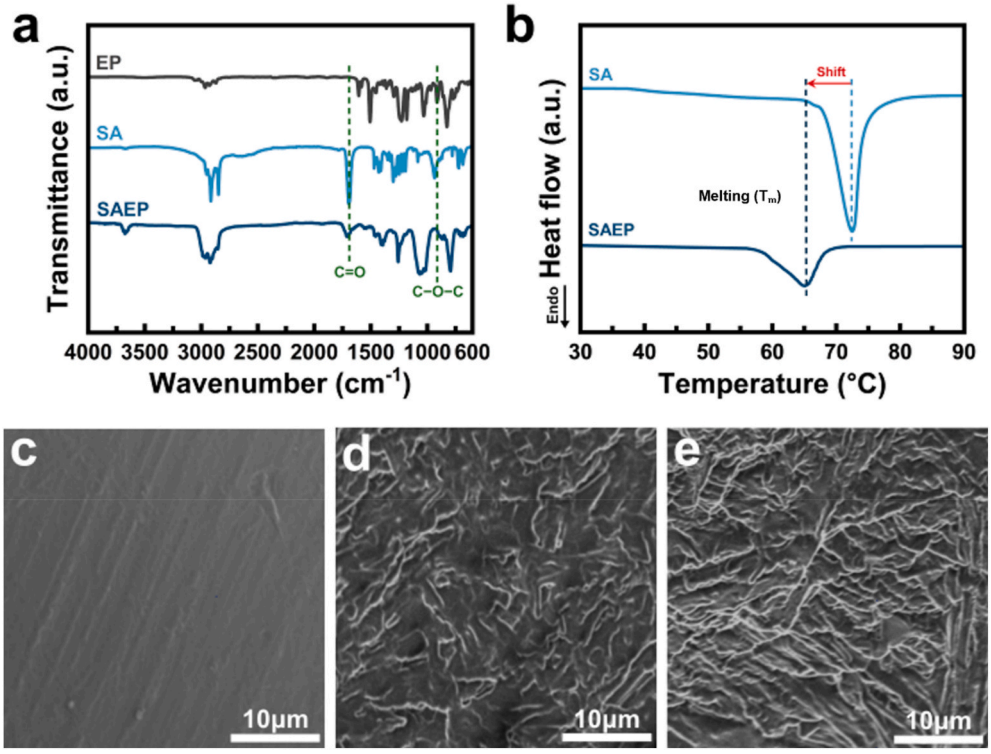


Fig. 2. FT-IR (a), DSC (b), and cross-sectional FE-SEM (c–e) analyses of EP, SA, and SAEP.

Table 1
Comparison of SAEP properties across varying ratios.

Ratio (SA: EP)	Tensile Strength (MPa)	Elongation at break (%)	Latent heat (J/g)
1:0 (pure SA)	0.62 ± 0.03	1.23 ± 0.04	221.4 ± 6.2
1:2	4.54 ± 0.15	3.71 ± 0.11	46.85 ± 1.35
1:1	3.07 ± 0.07	2.94 ± 0.12	101.71 ± 2.04
1.5:1	2.44 ± 0.12	2.06 ± 0.05	130.81 ± 3.62
2:1	1.94 ± 0.04	1.64 ± 0.07	156.67 ± 4.23

3.2. Filler characterization

To identify the chemical interactions introduced by CS functionalization, FT-IR and XPS analyses were performed. The FT-IR spectra in Fig. 3(a) present a comparison of pristine BN, pure CS, and the CBN, providing clear evidence of bonding changes. Pristine BN exhibited its characteristic in-plane B–N stretching and out-of-plane B–N bending modes at 1284 cm^{-1} and 792 cm^{-1}, respectively [28]. In contrast, CS exhibited a broad O–H/N–H stretching band centered at 3395 cm^{-1} and an $–NH_2$ bending vibration at 1596 cm^{-1} [29]. After ball milling BN with CS, the resulting CBN sample displayed notable spectral variations. The

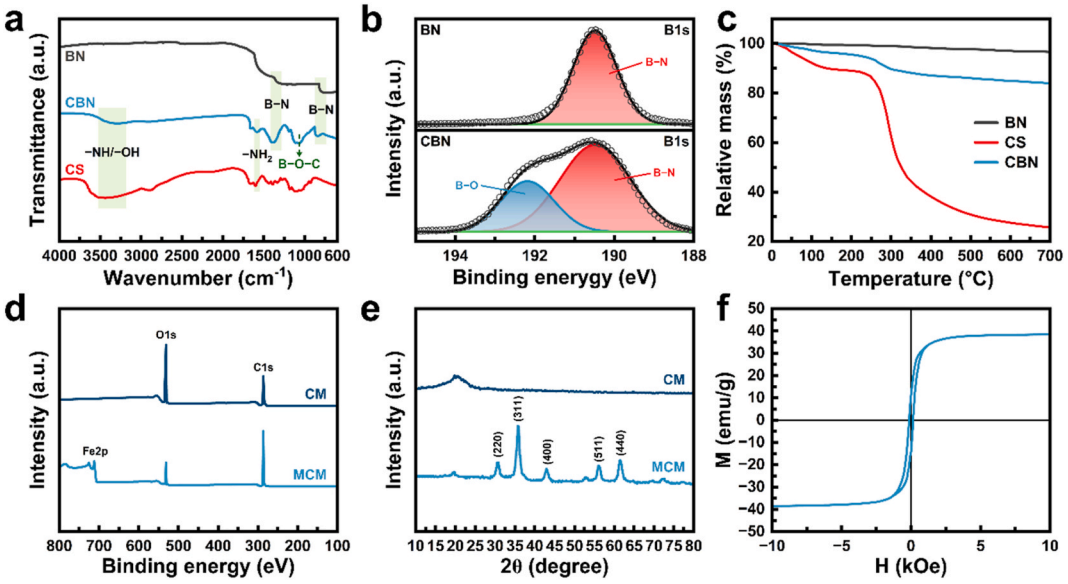


Fig. 3. (a) FT-IR spectra of BN, CS, and CBN. (b) XPS B 1s spectra of BN and CBN. (c) TGA curves of BN, CS, and CBN. (d, e) XPS survey spectra and XRD patterns of CM and MCM. (f) Magnetic hysteresis loop of MCMs.

B–N stretching and bending peaks shifted to 1367 cm^{-1} and 813 cm^{-1}, indicating lattice distortion caused by interactions with CS. A new absorption peak appeared at 1068 cm^{-1}, which is attributed to B–O–C stretching vibrations, consistent with the formation of boronate ester linkages between CS hydroxyl groups and surface boron atoms [30]. Additional CS-related features, including the broad band at 3200–3600 cm^{-1} (O–H/N–H stretching) and the peak near 1650 cm^{-1} (–NH_2 bending), further verify the presence of CS on the BN surface. These findings are corroborated by the XPS data (Fig. 3(b)). The B 1s spectrum of pristine BN displayed a dominant peak at 190.4 eV, characteristic of B–N bonding. After functionalization, an additional component at 192.1 eV appeared in the CBN spectrum, corresponding to B–O bonds originating from the formation of B–O–C linkages [31]. This B–O signal, which is absent in pristine BN, provides direct evidence of successful covalent attachment. Thermogravimetric analysis (TGA) was performed to quantify the amount of CS grafted onto the BN surface (Fig. 3(c)). While pristine BN exhibited virtually no weight loss up to 700 °C, CBN exhibited gradual mass loss beginning around 300 °C, which is attributed to the decomposition of grafted CS chains. The residual mass of CBN at 700 °C was 84.1%, indicating that approximately 15.9 wt% of CS was incorporated. Overall, these FT-IR, XPS, and TGA results demonstrate that CS-assisted ball milling enabled simultaneous exfoliation and covalent functionalization of BN, thereby enhancing its dispersion and compatibility within the SAEP matrix.

Following the chemical characterization of CBN, the properties of the MCMs were examined using XPS, XRD, and magnetic hysteresis analysis (Fig. 3(d–f)). The XPS survey spectrum (Fig. 3(d)) revealed clear compositional changes associated with carbonization and Fe_3O_4 incorporation. Compared to the precursor CMs, the MCMs exhibited a substantially higher C 1s signal and a lower O 1s contribution, consistent with the formation of a carbon-rich framework. Furthermore, new Fe-related peaks (Fe 2p) emerged in the spectrum, confirming the successful introduction of Fe_3O_4 nanoparticles into the microsphere structure. XRD analysis further verified the incorporation of Fe_3O_4 (Fig. 3(e)). Distinct diffraction peaks corresponding to the (220), (311), (400), (511), and (440) planes of magnetite (Fe_3O_4, JCPDS No. 19-0629) were observed [32], d demonstrating that crystalline Fe_3O_4 was effectively embedded within the carbon microspheres. The presence of these characteristic reflections indicates that the magnetization process was successful and that Fe_3O_4 retained its crystalline identity after integration. The magnetic hysteresis curve shown in Fig. 3(f) confirms that the MCMs possessed well-defined magnetic responsiveness [33]. The clear hysteresis behavior demonstrates that Fe_3O_4 nanoparticles impart magnetic functionality to the microspheres, which is advantageous for enhancing electromagnetic-wave attenuation through magnetic-loss mechanisms in subsequent EMI-shielding evaluations. These combined XPS, XRD, and magnetic measurements verify the effective incorporation of Fe_3O_4 into the carbon microspheres to produce magnetically active MCM fillers suitable for improving both thermal and electromagnetic performance in SAEP-based composites.

The morphology of the fillers was characterized via FE-SEM, as shown in Fig. 4. The CBN particles (Fig. 4(a)) displayed a smaller lateral size of approximately 4 μm compared to raw BN (12 μm), along with minor edge defects generated during the CS-assisted ball-milling process. These features indicate partial exfoliation and surface activation of BN. The MCMs appeared as spherical particles with diameters of 3–5 μm in the low-magnification SEM image (Fig. 4(b)). The corresponding high-magnification image (Fig. 4(c)) revealed a porous structure, which originated from the dissolution–regeneration process of cellulose during microsphere formation and was retained after carbonization. This pore network allowed the Fe_3O_4 nanoparticles to diffuse into and fill the voids of the carbon microspheres. The elemental mapping of Fe (Fig. 4(d)) confirmed the uniform distribution of Fe_3O_4 within the microspheres, verifying its effective infiltration into the porous carbon framework and the successful formation of MCMs.

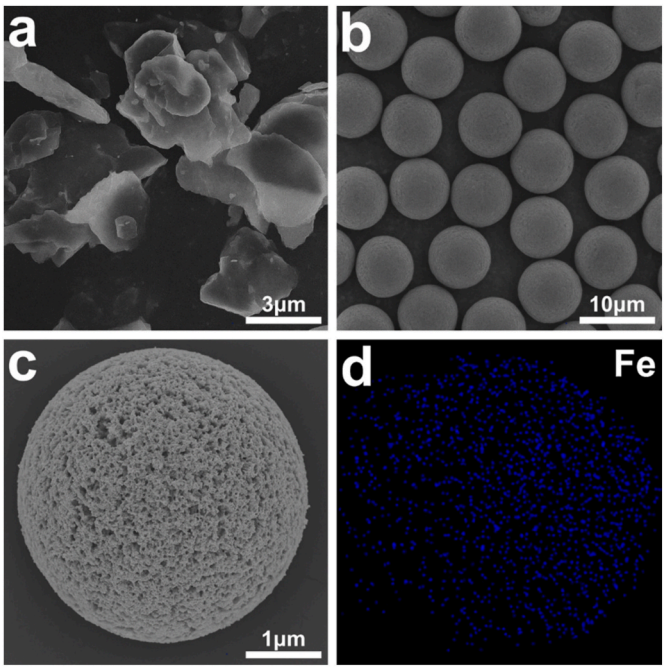


Fig. 4. Morphologies of (a) CBN and the MCMs at (b) low magnification and (c) high magnification. (d) EDS profile of the MCMs.

3.3. Morphology of the composites

To investigate the internal architecture of the composites, cross-sectional FE-SEM images of SAEP-based samples with different filler configurations were examined (Fig. 5). The SAEP/MCM composite (Fig. 5(a)) exhibited a uniform cross section, in which the spherical MCM particles were well dispersed within the matrix, forming a consistent microstructure without notable agglomeration. When CBN was incorporated at an MCM:CBN ratio of 2:1 (Fig. 5(b)), thin CBN

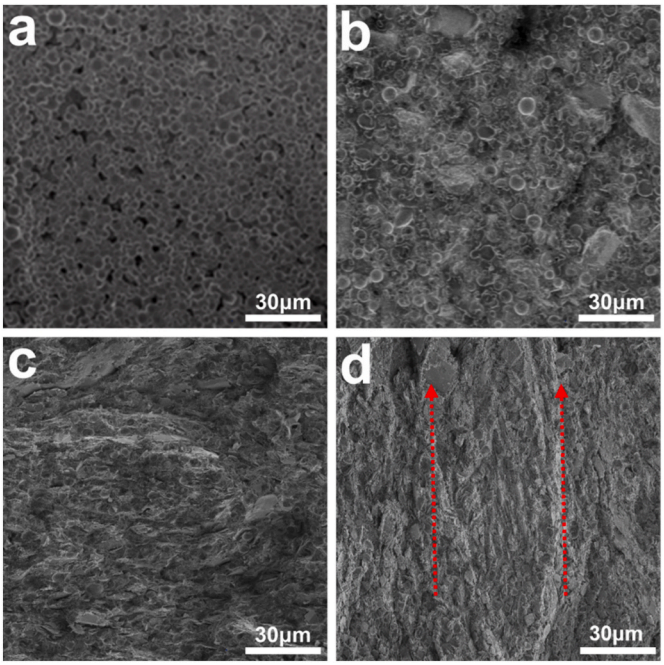


Fig. 5. Cross-sectional FE-SEM images of SAEP-based composites with different filler configurations: (a) SAEP/MCM, (b) SAEP/MCM/CBN (2:1), (c) SAEP/MCM/CBN (1:1), (d) SAEP/MCM/CBN (1:2).

platelets appeared between the MCM particles and were mainly aligned in the in-plane direction, reflecting the natural orientation tendency of two-dimensional (2D) fillers during pressing. At an equal filler ratio of 1:1 (Fig. 5(c)), the distribution of the MCMs and CBN became more balanced, producing a partially interconnected microstructure where CBN flakes began to bridge between neighboring MCM domains. As the CBN content increased (1:2, Fig. 5(d)), CBN platelets densely surrounded the spherical MCM particles, forming vertically connected filler networks that facilitate efficient through-plane heat-transfer pathways. This structural arrangement is advantageous for enhancing through-plane thermal conductivity in PCM composites.

3.4. EMI shielding performance of the composites

The EMI shielding performance of the SAEP/MCM/CBN composites in the 8.2–12.4 GHz range is presented in Fig. 6(a). The total SE (SE_T) of all samples increased with filler loading. Notably, the SAEP/MCM/CBN (2:1) composite exhibited the highest SE_T value of 65.2 dB, which exceeds the commonly accepted criterion of 20 dB. The SE_T was determined using the relationship [34]:

$$SE_T = SE_R + SE_A + SE_M \quad (1)$$

where SE_R, SE_A, and SE_M represent reflection, absorption, and multiple-reflection contributions, respectively. Generally, when SE_T exceeds about 15 dB, the contribution of multiple reflections becomes minimal; therefore, SE_M was regarded as negligible for all composite samples. As shown in Fig. 6(b), SE_A was consistently higher than SE_R across all compositions. Moderate frequency-dependent variations in EMI shielding effectiveness are observed within the X-band, which can be attributed to the frequency-dependent contributions of conduction loss in the carbon framework, magnetic loss associated with Fe_3O_4 nanoparticles, and interfacial polarization at the MCM–CBN–SAEP interfaces. In addition, multiple scattering within the porous MCM structure may slightly modulate the effective attenuation path length across the measured frequency range.

These values indicate the relative contributions of reflection and absorption components to the SE_T; however, they do not directly define the shielding mechanism. To identify the dominant shielding mechanism, the absorption (A), reflection (R), and transmission (T) coefficients were calculated based on the energy conservation relationship $A + R + T = 1$, and the results are shown in Fig. 6(c). The SAEP/MCM/CBN (2:1) composite exhibited the highest absorption coefficient and the lowest transmission, demonstrating that its EMI shielding behavior is governed by an absorption-dominant mechanism. The absorption-dominant EMI shielding behavior arises from the synergistic interplay between magnetic loss induced by Fe_3O_4 nanoparticles and conductive and dielectric losses within the carbon framework. The magnetic component promotes attenuation through resonance-related and current-induced losses, while the interconnected carbon network facilitates charge transport, interfacial polarization, and repeated internal scattering of electromagnetic waves. The combined magnetic and dielectric dissipation processes effectively convert incident electromagnetic energy into thermal energy, thereby enhancing absorption-dominated shielding. Since A, R, and T directly represent the redistribution of incident electromagnetic energy, these coefficients provide an appropriate basis for mechanistic interpretation.

The pronounced absorption behavior observed in the MCM-rich composite is primarily attributed to the characteristics of the MCM filler. The carbonized microsphere framework forms continuous dissipative pathways that promote conduction loss, while the Fe_3O_4 nanoparticles inside the microspheres introduce magnetic-loss channels that further attenuate incoming electromagnetic waves. In addition, the spherical geometry of the MCM induces internal multiple scattering, extending the propagation path and increasing the likelihood of energy dissipation. Although CBN introduces additional interfaces capable of inducing polarization loss, its influence is secondary when compared to the dominant conductive and magnetic functions of the MCMs. Overall, the SAEP/MCM/CBN composites demonstrate effective EMI shielding, and the highest SE_T observed in the 2:1 composite formulation is closely associated with its absorption-dominant behavior, as revealed by the A, R, and T coefficients. The combined conductive carbon framework and magnetic-loss characteristics of the MCMs play a central role in achieving this enhanced shielding performance. Although the electrical conductivity increases with filler loading (Fig. S2), the EMI shielding behavior of the composites is dominated by absorption loss due to the synergistic combination of conductive networks and magnetic fillers, which enhances dielectric polarization and magnetic loss rather than surface reflection. All SAEP/MCM/CBN composite samples were prepared with a uniform thickness of 1.8 mm for electrical conductivity and EMI shielding measur where SE_R, SE_A, and SE_M represent reflection, absorption, and multiple-reflection contributions, respectively. Generally, when SE_T exceeds about 15 dB, the contribution of multiple reflections becomes minimal; therefore, SE_M was regarded as negligible for all composite samples. As shown in Fig. 6(b), SE_A was consistently higher than SE_R across all compositions. These values indicate the relative contributions of reflection and absorption components to the SE_T; however, they do not directly define the shielding mechanism. To identify the dominant shielding mechanism, the absorption (A), reflection (R), and transmission (T) coefficients were calculated based on the energy conservation relationship $A + R + T = 1$, and the results are shown in Fig. 6(c). The power coefficients were calculated from the measured S-parameters following the ASTM D4935 standard. The effect of multiple internal reflections was neglected, as the absorption shielding effectiveness (SE_A) exceeded 10 dB. The SAEP/MCM/CBN (2:1) composite exhibited the highest absorption coefficient and the lowest transmission, demonstrating that its EMI shielding behavior is governed by an absorption-dominant mechanism. Since A, R, and T directly represent the redistribution of incident electromagnetic energy, these coefficients provide an appropriate basis for mechanistic interpretation.

The pronounced absorption behavior observed in the MCM-rich composite is primarily attributed to the characteristics of the MCM

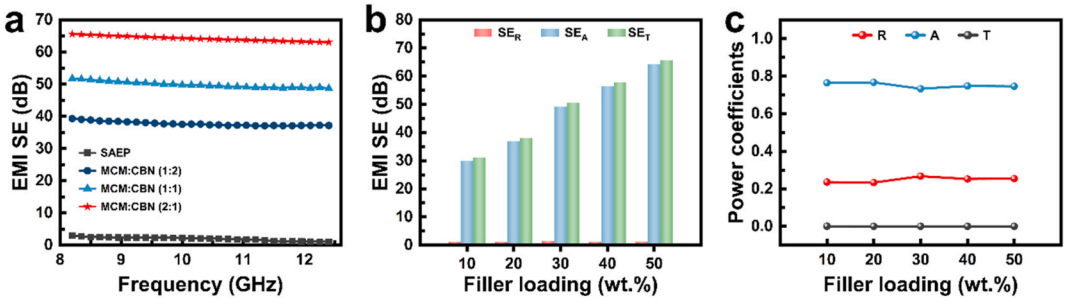


Fig. 6. (a) EMI SE of SAEP/MCM/CBN composites with different MCM:CBN ratios in the 8.2–12.4 GHz range. Impact of filler loading on (b) SE_R, SE_A, and SE_T EMI shielding components, and (c) the corresponding power coefficients (R, A, and T) for the SAEP/MCM/CBN (2:1) composite.

filler. The carbonized microsphere framework forms continuous dissipative pathways that promote conduction loss, while the Fe_3O_4 nanoparticles inside the microspheres introduce magnetic-loss channels that further attenuate incoming electromagnetic waves. In addition, the spherical geometry of the MCM induces internal multiple scattering, extending the propagation path and increasing the likelihood of energy dissipation. Although CBN introduces additional interfaces capable of inducing polarization loss, its influence is secondary when compared to the dominant conductive and magnetic functions of the MCMs. Overall, the SAEP/MCM/CBN composites demonstrate effective EMI shielding, and the highest SE_T observed in the 2:1 composite formulation is closely associated with its absorption-dominant behavior, as revealed by the A, R, and T coefficients. The combined conductive carbon framework and magnetic-loss characteristics of the MCMs play a central role in achieving this enhanced shielding performance. Although the electrical conductivity increases with filler loading (Fig. S2), the EMI shielding behavior of the composites is dominated by absorption loss due to the synergistic combination of conductive networks and magnetic fillers, which enhances dielectric polarization and magnetic loss rather than surface reflection. All SAEP/MCM/CBN composite samples were prepared with a uniform thickness of 1.8 mm for electrical conductivity and EMI shielding measurements.

3.5. Thermal properties of the composites

The thermal properties of the SAEP/MCM/CBN composites are summarized in Fig. 7. The through-plane thermal conductivity is presented in Fig. 7(a). All measurements were conducted under identical system configurations and operating conditions to enable a direct comparison of relative temperature reduction among different TIM samples. The pristine SAEP matrix exhibited a low thermal conductivity of approximately 0.23 W m^{-1} K^{-1}, whereas the incorporation of MCM and CBN markedly enhanced heat-transfer capability. Among all tested formulations, the SAEP/MCM/CBN (2:1) composite achieved the highest thermal conductivity of 5.11 W m^{-1} K^{-1}, demonstrating a substantial improvement over pristine SAEP. This enhancement correlates well with the cross-sectional FE-SEM observations, which revealed a pronounced through-plane alignment of MCM and CBN fillers in the SAEP/MCM/CBN 2:1 composite. The carbonized MCM framework, enriched with magnetic Fe_3O_4 nanoparticles, provides interconnected conduction pathways, while the CBN flakes bridge these pathways and reduce phonon-scattering gaps. Furthermore, hot-press densification minimizes interfacial voids, enabling more efficient phonon transport and ultimately contributing to the markedly increased through-plane thermal conductivity.

To provide a clearer quantitative comparison across compositions, the thermal conductivity enhancement was calculated as follows [35]:

$$TCE = \frac{\lambda - \lambda_m}{\lambda_m} \tag{2}$$

where λ and λ_m are the thermal conductivities of the composite and pristine SAEP, respectively (Fig. 7(b)). The thermal conductivity enhancement consistently increased as the MCM content increased, mirroring the behavior of the absolute thermal conductivity. Notably, the SAEP/MCM/CBN (2:1) composite demonstrated the highest thermal conductivity enhancement value of 2122%, confirming the dominant contribution of the conductive–magnetic MCM network to the overall heat-transfer enhancement.

The phase-transition and latent-heat properties of the composites were evaluated using DSC (Fig. 7(c)). The pristine SAEP matrix displayed a clear endothermic peak near 65 °C due to the melting of chemically bonded SA segments. As the filler loading increased, the latent heat gradually decreased because of the reduced PCM fraction. Nevertheless, the optimized SAEP/MCM/CBN composite maintained a latent heat of 90.5 J g^{-1}, indicating that the hybrid filler network enhances heat conduction without severely compromising energy-storage capability. The corresponding latent-heat values are summarized in Fig. 7(d), which displays the balance between thermal conductivity and latent heat across different filler contents. Achieving both high thermal conductivity and adequate latent heat remains challenging for PCM composites; however, the SAEP/MCM/CBN (2:1) composite offers a balanced combination of both properties, demonstrating its suitability for heat-saving and heat-dissipation applications. Cycling stability was examined through repeated DSC measurements over 100 heating–cooling cycles (Fig. 7(e)). After cycling, the latent heat decreased by only 2.1%, indicating that the SAEP/MCM/CBN composite maintains excellent phase-transition stability with negligible degradation during repeated operation.

For broader context, Fig. 7(f) compares the thermal conductivity and EMI SE of the SAEP/MCM/CBN composites with those reported for

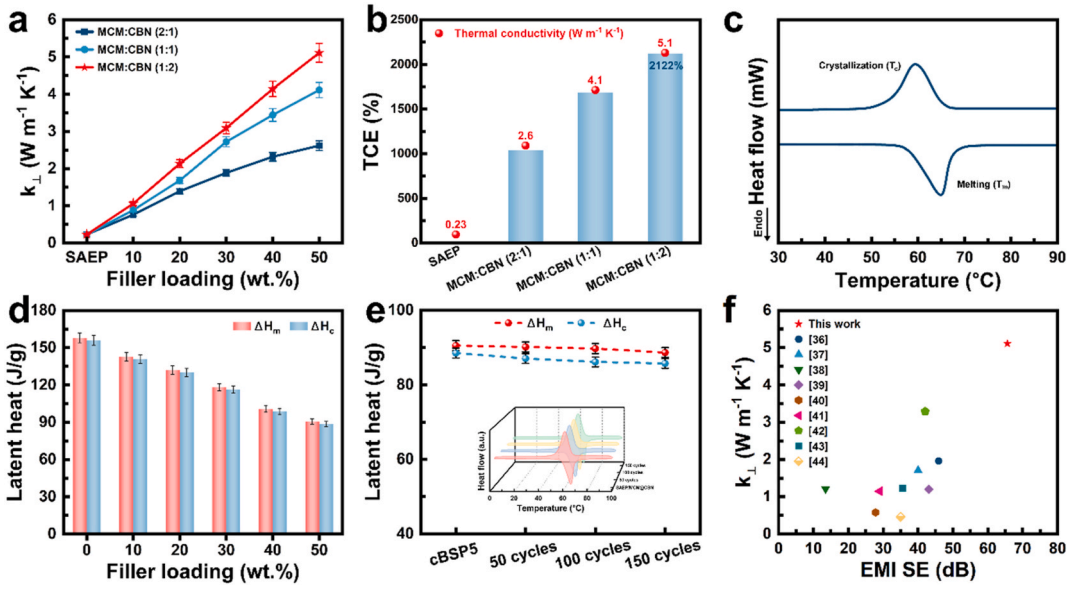


Fig. 7. (a) Through-plane TC at various filler loadings. (b) thermal conductivity enhancement relative to pristine SAEP. (c) DSC curves of the SAEP/MCM/CBN. (d) Latent heat values (ΔH_m, ΔH_c) as a function of filler loading. (e) Latent-heat retention during repeated DSC cycling. (f) Comparison of TC and EMI SE with previously reported materials. (Error bars represent the standard deviation calculated from 5 independent measurements.)

recent thermal-management materials [36–44]. The SAEP/MCM/CBN system exhibits superior integrated performance, achieving high through-plane thermal conductivity, stable phase-change behavior, and effective EMI shielding. These results highlight its tremendous potential for next-generation TIMs and energy-storage applications see (Fig. 9).

3.6. Leakage behavior and mechanical properties of SAEP/MCM/CBN

The thermal leakage resistance of the SAEP/MCM/CBN composites was evaluated through the leakage test illustrated in Fig. 8(a), and the corresponding retention rate values are presented in Fig. 8(b). The retention (ε) and leakage (γ) rates were calculated using Eqs. (3) and (4) [45]:

$$\varepsilon = \frac{m_r}{m_0} \times 100\% \tag{3}$$

$$\gamma = \left(1 - \frac{m_r}{m_0}\right) \times 100\% \tag{4}$$

where m_0 represents the initial mass of the sample, and m_r denotes the remaining mass after heating. These metrics serve as quantitative indicators of structural integrity and confinement capability during thermal exposure. Pure SAEP exhibited a decline in retention once the temperature exceeded its melting range, reflecting the intrinsic mobility of the molten phase. The primary improvement in leakage resistance was due to the formation of a chemically bonded epoxy–ester network, which substantially enhanced the structural rigidity of the matrix and prevented PCM flow during melting. When the fillers were introduced, the stability was further reinforced. Although chemical cross-linking played the dominant role in suppressing leakage, the presence of MCMs provided an additional stabilizing effect. The internal cavities within the MCM particles allowed a portion of the SAEP matrix to become mechanically anchored during fabrication, contributing to a secondary confinement mechanism. Consequently, the SAEP/MCM/CBN composite exhibited substantially improved thermal-form stability, maintaining complete leakage resistance up to 110 °C, which is well above the melting temperature of SA.

The mechanical performance of the composites was characterized using a universal testing machine, as shown in Fig. 7(c) and (d). Compared to pure SAEP, the SAEP/MCM/CBN composite demonstrated considerably higher tensile strength and elongation at break. This improvement stems from the combined reinforcing effect of the rigid CBN flakes and the robust carbon framework of the MCMs, which collectively form a mechanically interconnected network within the polymer matrix. Composites with higher CBN ratios demonstrated superior tensile properties due to the continuous alignment of 2D CBN platelets, which enhanced load transfer and minimized localized stress concentrations. Overall, the incorporation of both MCMs and CBN as hybrid fillers endowed the composites with excellent leakage resistance and substantially improved mechanical durability, underscoring their suitability for high-performance PCM applications.

3.7. Thermal management performance of SAEP/MCM/CBN

Infrared thermal imaging was performed to visualize the heat-transfer behavior of the SAEP/MCM/CBN composites, and the results are presented in Fig. 8(a). For this analysis, four representative samples were simultaneously placed on a heating plate maintained at 60 °C. Sequential infrared images captured at 1, 3, 5, 10, and 15 s revealed clear differences in dynamic thermal response among the samples. The SAEP/MCM/CBN (1:2) composite exhibited the fastest rise in surface temperature, whereas the pure SAEP heated at a noticeably slower rate. These observations directly reflect the enhanced vertical heat-transfer pathways produced by the hybrid MCM–CBN filler network. The corresponding surface temperature profiles in Fig. 8(b) further quantify these differences. At 15 s, the surface temperature of SAEP/MCM/CBN (1:2) reached 56.9 °C, which was significantly higher than that of the pure SAEP (42.1 °C). This rapid temperature response confirms that the

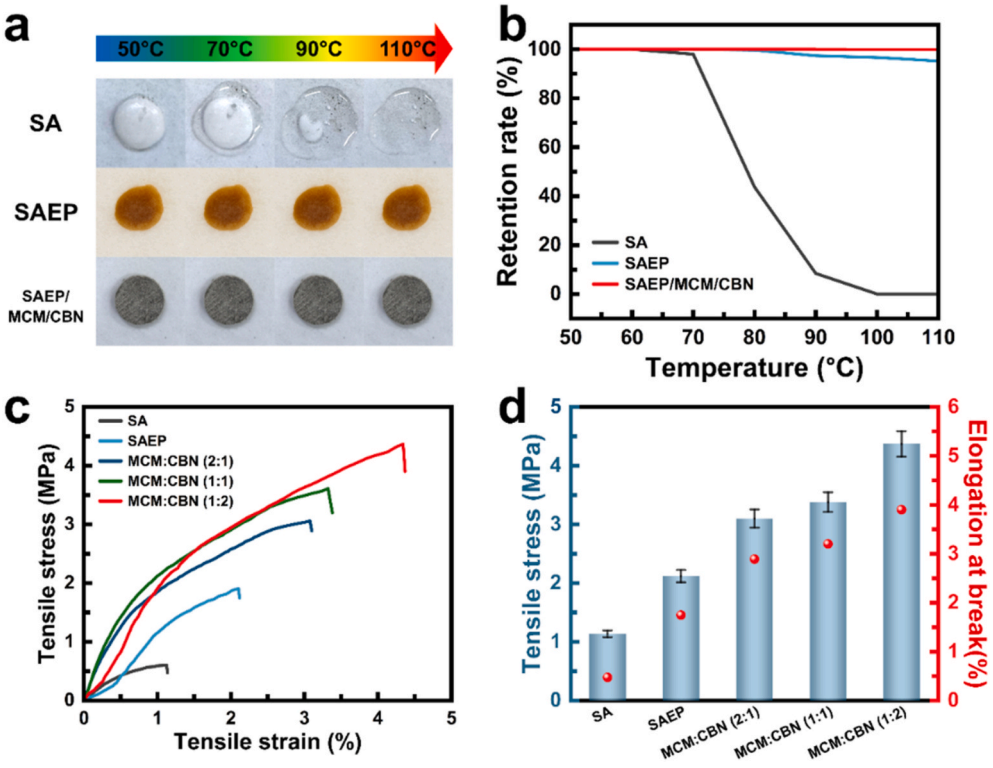


Fig. 8. (a) Thermal leakage test images. (b) Retention rates. (c) Tensile stress–strain curves. (d) Tensile strength and elongation-at-break of SA, SAEP, and SAEP/MCM/CBN composites. (Error bars represent the standard deviation calculated from 5 independent measurements.)

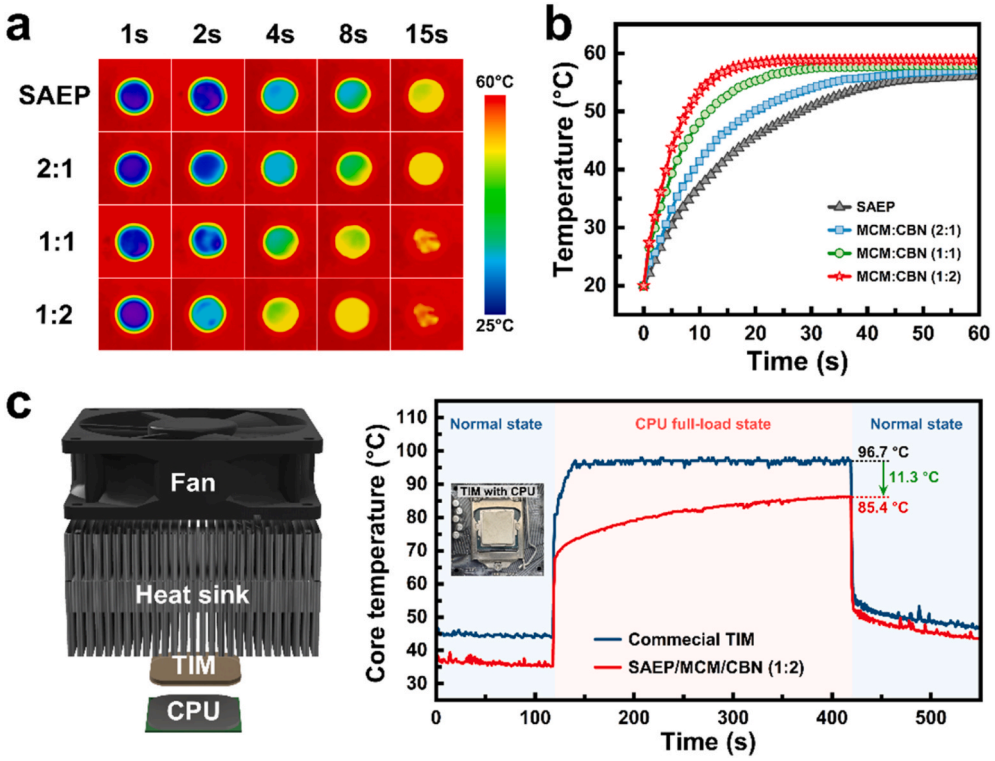


Fig. 9. (a) Infrared thermal images of the SAEP/MCM/CBN composites on a 60 °C hot plate. (b) Surface temperature profiles over time. (c) CPU thermal management test using SAEP/MCM/CBN (1:2) as a TIM and comparison of the CPU core temperature with that of a commercial TIM.

combined effect of spherical MCM particles and 2D CBN platelets promotes efficient through-plane conduction, enabling rapid heat propagation from the heating plate to the top surface. Such enhanced thermal response is particularly advantageous for PCM applications, as it directly translates into increased thermal charging/discharging rates.

To further evaluate its practical heat-dissipation capability, the SAEP/MCM/CBN composite was tested as a TIM in a real CPU setup. As shown in Fig. 8(c), the composite film (70 μm thickness) was positioned between a CPU (Intel Core i5-9500F) and an aluminum heat sink. For comparison, a commercial TIM (ARCTIC MX-4) was used under identical hardware and environmental conditions. The system was subjected to a 100% CPU load using OCCT, and the real-time core temperature was recorded with AIDA64. The SAEP/MCM/CBN TIM demonstrated superior thermal-management performance throughout the stress test, consistently maintaining lower CPU temperatures than the commercial TIM. It reduced the maximum core temperature by approximately 11.3 °C, highlighting its exceptional heat-spreading capability. This improvement results from the synergistic thermal-regulation mechanism of the SAEP/MCM/CBN structure: the interconnected CBN network enables rapid through-plane heat conduction from the CPU to the heat sink, while the SAEP-based PCM matrix absorbs excess heat through latent heat storage, effectively buffering transient thermal spikes during sudden load increases.

Collectively, these results confirm the strong potential of SAEP/MCM/CBN composites as next-generation TIMs. Their ability to combine efficient heat conduction, rapid thermal response, and phase-change-driven heat buffering within a mechanically robust matrix offers a versatile and practical thermal-management solution for high-performance electronic systems.

4. Conclusion

In this study, a multifunctional composite system was developed by incorporating MCMs and CBN into a chemically bonded SAEP matrix. The formed SAEP network provided a stable and leakage-resistant PCM framework, while the hybrid fillers contributed to improvements in thermal, mechanical, and electromagnetic performance. The MCMs, composed of carbon microspheres embedded with Fe_3O_4 nanoparticles, provided both conductive and magnetic characteristics, while CBN offered high thermal conductivity and mechanical reinforcement. Owing to the complementary roles of these fillers, the SAEP/MCM/CBN composite exhibited a through-plane thermal conductivity of 5.11 W m^{-1} K^{-1}, demonstrating a dramatic improvement over the pristine SAEP, and it maintained a latent heat of 90.5 J g^{-1} even at high filler loadings. The composite also demonstrated strong thermal-form stability, retaining its structure without leakage up to 110 °C, which is substantially above the melting range of SA segments.

EMI measurements confirmed that the SAEP/MCM/CBN composites exhibited effective shielding behavior, primarily governed by absorption, with the 2:1 formulation delivering the highest SE_T value among the tested samples. This high performance is attributable to the conductive carbon framework and magnetic Fe_3O_4 domains within MCMs, which promote attenuation of incident electromagnetic waves. Mechanical testing further revealed that the incorporation of MCMs and CBN enhanced both tensile strength and elongation at break, resulting in improved structural robustness. The rigid CBN flakes and MCM framework jointly contributed to load transfer and suppressed stress concentration within the matrix. Overall, the SAEP/MCM/CBN composites achieved a well-balanced combination of enhanced thermal conduction, stable phase-change behavior, strengthened mechanical performance, and effective EMI shielding, demonstrating their strong potential for next-generation thermal-management and functional composite applications.

CRediT authorship contribution statement

Jaekyung Lee: Conceptualization, Data curation, Formal analysis, Investigation, Methodology, Writing – original draft. **Jaeyeon Kim:** Formal analysis, Investigation, Writing – review & editing. **Oju Kwon:** Data curation, Formal analysis. **Subin Lee:** Data curation, Formal

analysis. **Pei-Chen Su:** Formal analysis, Supervision. **Jooheon Kim:** Funding acquisition, Project administration, Supervision.

Acknowledgement

This research was supported by the National Research Foundation of Korea (NRF) grant funded by the Korea government (MSIT) (RS-2024-00350658) and supported by the IITP (Institute of Information & Coummunications Technology Planning & Evaluation)-ITRC (Information Technology Research Center) (IITP-2025-RS-2020-II201655, 30%) grant funded by the Korea government (Ministry of Science and ICT).

Appendix A. Supplementary data

Supplementary data to this article can be found online at https://doi.org/10.1016/j.polymertesting.2026.109127.

Data availability

Data will be made available on request.

References

[1] Y. Bai, S. Wang, G. Wang, Y. Lu, L. Liang, X. Mei, S. Wang, C. Guo, J. Jiao, X. Shi, S. Zhang, Crosslinked carbon nanotube/crystalline PEEK composites for high strength and electromagnetic interference shielding under harsh environments, Carbon N. Y. 242 (2025), https://doi.org/10.1016/j.carbon.2025.120448.

[2] Y. Xiao, J. Lin, Y. Cao, X. Liu, H. Wang, S. Alshammari, X. Shi, H. Guo, M.H. Helal, H. Algadi, J. Ren, N. Zhumanova, N. Akimbayeva, Z. Toktarbay, J. Huang, Z. Guo, Coaxial electrospun PEG-4000@PVDF composite membranes with intumescent flame retardants: toward multifunctional fabrics for thermal management and ultra-safe lithium-ion battery separators, J. Mater. Sci. Technol. 251 (2026) 282–296, https://doi.org/10.1016/j.jmst.2025.07.004.

[3] X. Wang, X. Hu, Z. Liu, C. Zhu, R. Shen, B. Quan, X. Yan, W. Wang, X. Lu, J. Qu, Interpenetrating double-network ANF/MXene-K+ aerogels enable integrated electromagnetic interference shielding, infrared camouflage, and Joule Heating in adaptive multifunctional systems, Nano Res. 18 (2025), https://doi.org/10.26599/NR.2025.94907702.

[4] C. Zhu, Y. Hao, H. Wu, M. Chen, B. Quan, S. Liu, X. Hu, S. Liu, Q. Ji, X. Lu, J. Qu, Self-assembly of binderless MXene aerogel for multiple-scenario and responsive phase change composites with ultrahigh thermal energy storage density and exceptional electromagnetic interference shielding, Nano-Micro Lett. 16 (2024), https://doi.org/10.1007/s40820-023-01288-y.

[5] Y. Rong, H. Guo, X. Zhou, W. Wu, W. Zhu, H. Wang, X. Ma, S. Jiang, Q. Sun, Absorption-dominant electromagnetic interference shielding materials: from microstructure to multi-scale assembly, Adv. Funct. Mater. (2025), https://doi.org/10.1002/adfm.202506746.

[6] T. Hwang, W. Lee, P.C. Su, J. Kim, Development of recyclable vitrimeric phase change material composites with high thermal conductivity and stability for advanced thermal management, J. Energy Storage 140 (2025), https://doi.org/10.1016/j.est.2025.119070.

[7] S.J. Ha, H.J. Jang, H. jin Son, Y.K. Moon, H.A. Cha, J.J. Choi, J.H. Ahn, B.D. Hahn, K.H. Cho, D.C. Ahn, J. Lim, S.C. Jeon, I.C. Jung, Y. Song, H. Zhou, T. Feng, C. W. Ahn, Advanced thermal interface materials: insights into low-temperature sintering and high thermal conductivity of MgO, Adv. Mater. (2025), https://doi.org/10.1002/adma.202510237.

[8] Z. Liu, J. Wang, G. He, Z. Yang, Engineering the thermal conductivity of polymer-bonded explosives by interfacial thermal resistance reduction and structural designs: a review, Adv. Compos. Hybrid Mater. 8 (2025), https://doi.org/10.1007/s42114-024-01076-1.

[9] R. Hu, S. Wen, Q. Chen, X. Sun, H. Liu, W. Gao, Y. Bai, Universal construction of electrical insulation and high-thermal-conductivity composites based on the in situ exfoliation of boron nitride-graphene hybrid filler, ACS Appl. Mater. Interfaces 17 (2025) 6783–6792, https://doi.org/10.1021/acsami.4c18250.

[10] W. Yang, J. Kim, P.C. Su, J. Kim, Improving the thermal conductivity of an epoxy composite with chemically boron nitride-grafted carbon fiber, Compos. Part A Appl. Sci. Manuf. 182 (2024), https://doi.org/10.1016/j.compositesa.2024.108192.

[11] J. Cho, E. Jang, J. Kim, J. Kim, Enhanced thermal conductivity and insulating properties of PBO fiber grafted AlN/BN/PBO films for electronic packaging, Ceram. Int. 51 (2025) 2155–2162, https://doi.org/10.1016/j.ceramint.2025.11.192.

[12] D. Lin, Y. Pu, Z. Peng, Y. Feng, Q. Li, Construction of AlN@Al2O3 core-shell structure for achieving high thermal conductivity and low dielectric loss of PTFE-based composites, J. Alloys Compd. 1036 (2025), https://doi.org/10.1016/j.jallcom.2025.182156.

[13] S. Kim, W. Lee, J. Lee, J. Kim, Multifunctional PCM composites for thermal management based on TiO2-Grown carbonized cotton and acetamide grafted Bisphenol-A, Carbon N. Y. 247 (2026), https://doi.org/10.1016/j.carbon.2025.121038.

[14] M. Li, S. Han, C. Dan, T. Wu, F. You, X. Jiang, Y. Wu, Z.M. Dang, Boron nitride-polymer composites with high thermal conductivity: preparation, functionalization strategy and innovative structural regulation, Small 21 (2025), https://doi.org/10.1002/smll.202412447.

[15] L. Zhang, X. Ding, D. Lin, Y. Feng, H. Fu, G. Xiao, P. Xu, Q. Li, A porous electrically and thermally conductive composite film for heat dissipation and electromagnetic interference shielding, Compos. B Eng. 297 (2025), https://doi.org/10.1016/j.compositesb.2025.112339.

[16] Y. Ding, Q. Jiang, H. Lin, X. Liu, J. Zhou, D. Tang, J. Yi, J. Feng, Laminated architecture with interpenetrating 3D-Gr enhancement of strength and electrical conductivity in Cu matrix composites, J. Alloys Compd. 1044 (2025), https://doi.org/10.1016/j.jallcom.2025.184543.

[17] M. Kim, J. Kim, Enhancing filler ratio and thermal conductivity of polyphenylene sulfide composites using molybdenum sulfide and carbon nanotubes: a layer-by-layer hot-pressing approach, J. Mater. Res. Technol. 33 (2024) 2756–2763, https://doi.org/10.1016/j.jmrt.2024.09.253.

[18] S.B. Cho, J. Lee, K.C. Dimitrov, Y. Lee, D.Y. Khang, Symmetric Fe3O4/PEDOT:PSS/Fe3O4 sandwich layers for high performance absorption-dominated electromagnetic interference shielding, Surf. Interfaces 76 (2025), https://doi.org/10.1016/j.surfin.2025.107924.

[19] J. Lee, J. Kim, O. Kwon, S. Lee, P.C. Su, J. Kim, Vertically aligned hollow Ag@Ni tubes for synergistic EMI shielding and enhancing the thermal conductivities of epoxy composites, Appl. Mater. Today 44 (2025), https://doi.org/10.1016/j.apmt.2025.102741.

[20] Y. Lin, K. Yu, J. Chen, B. Zhang, W. Chen, Y. Yu, Multifunctional pompon chrysanthemum-like boron nitride microsphere/carbon fiber@cobalt heterostructured composites toward highly-efficient microwave absorption and electromagnetic interference shielding, Chem. Eng. J. 510 (2025), https://doi.org/10.1016/j.cej.2025.161436.

[21] S. Kim, W. Lee, T. Hwang, J. Park, N. Lee, P.C. Su, J. Kim, Phase change material composites in a clay-like structure featuring GPTMS and butylated epoxy for heat buffering and thermal interface performance, J. Mater. Res. Technol. 39 (2025) 5573–5581, https://doi.org/10.1016/j.jmrt.2025.10.218.

[22] Y. Xiao, T. Li, Y. Yang, J. Lin, X. Sheng, J. Huang, T. Li, X. Lu, D. Xie, Exploring flame-retardant, shape-stabilized multi-functional composite phase change materials, Sol. Energy Mater. Sol. Cell. 282 (2025), https://doi.org/10.1016/j.solmat.2025.113369.

[23] G. Pan, Z. Du, C. Zhang, C. Li, X. Yang, H. Li, Effect of structure of bridging group on curing and properties of bisphenol-a based novolac epoxy resins, Polym. J. 39 (2007) 478–487, https://doi.org/10.1295/polymj.PJ2006201.

[24] P.D.A. Pudney, K.J. Mutch, S. Zhu, Characterising the phase behaviour of stearic acid and its triethanolamine soap and acid-soap by infrared spectroscopy, Phys. Chem. Chem. Phys. 11 (2009) 5010–5018, https://doi.org/10.1039/b819582j.

[25] Z. Huang, Q. Ye, Z. Shi, J.N. Tang, X. Ouyang, D.Z. Chen, Multiple phase change-stimulated shape memory and self-healing epoxy composites with thermal regulation function, Chem. Eng. J. 409 (2021), https://doi.org/10.1016/j.cej.2020.127382.

[26] J. Puig, I.E. Dell Erba, W.F. Schroeder, C.E. Hoppe, R.J.J. Williams, Epoxy-based organogels for thermally reversible light scattering films and form-stable phase change materials, ACS Appl. Mater. Interfaces 9 (2017) 11126–11133, https://doi.org/10.1021/acsami.7b00086.

[27] F. Mustata, N. Tudorachi, I. Bicu, The kinetic study and thermal characterization of epoxy resins crosslinked with amino carboxylic acids, J. Anal. Appl. Pyrolysis 112 (2015) 180–191, https://doi.org/10.1016/j.jaap.2015.01.030.

[28] S. Kong, H. Seo, H. Shin, J.H. Baik, J. Oh, Y.O. Kim, J.C. Lee, Improvement in mechanical and thermal properties of polypropylene nanocomposites using an extremely small amount of alkyl chain-grafted hexagonal boron nitride nanosheets, Polymer (Guildf). 180 (2019), https://doi.org/10.1016/j.polymer.2019.121714.

[29] H. Jafari, H. Namazi, Chitosan/laponite clay bio-nanocomposite as an efficient cytocompatible nanocarrier for pH-sensitive controlled release of curcumin, Inorg. Chem. Commun. 168 (2024), https://doi.org/10.1016/j.inoche.2025.112940.

[30] S. Chen, R. Xu, J. Liu, X. Zou, L. Qiu, F. Kang, B. Liu, H.M. Cheng, Simultaneous production and functionalization of boron nitride nanosheets by sugar-assisted mechanochemical exfoliation, Adv. Mater. 31 (2019), https://doi.org/10.1002/adma.201804810.

[31] J. Zhou, Y. Xiao, S. Liu, Z. Li, X. Liu, S. Zhang, Z. Li, Boric acid-regulated gelation and ethanol-assisted preparation of polybenzoxazine aerogels, Chem. Eng. J. 486 (2024), https://doi.org/10.1016/j.cej.2024.150228.

[32] B.M. Saloom, A.A. Al-Dergazly, Designing magnetic field filter based on no-core fiber assisted by a ferrofluid, Appl. Phys. B 131 (2025), https://doi.org/10.1007/s00340-024-08379-7.

[33] I. Collado, A. Vázquez-López, M. Fernández, J. de la Vega, A. Jiménez-Suárez, S. G. Prolongo, Nanocomposites of sequential dual curing of thiol-epoxy systems with Fe3O4 nanoparticles for remote/in situ applications: thermomechanical, shape memory, and induction heating properties, Adv. Compos. Hybrid Mater. 8 (2025), https://doi.org/10.1007/s42114-025-01264-7.

[34] C. Yuan, X. Li, M. Huang, F. Li, Z. Zhang, C. Wang, W. Hu, Multifunctional asymmetric foam with compression-enhanced EMI shielding effectiveness exhibits real-time tunability of reflection/absorption ratio and pressure sensing, Chem. Eng. J. 489 (2024), https://doi.org/10.1016/j.cej.2024.151359.

[35] J. Lee, J. Kim, O. Kwon, S. Lee, P.C. Su, J. Kim, Development of high-performance silk-based composite films with enhanced thermal conductivity and EMI shielding effectiveness, Polym. Compos. 46 (2025) 10173–10186, https://doi.org/10.1002/pc.29612.

[36] L. Han, K. Li, Y. Fu, X. Yin, Y. Jiao, Q. Song, Multifunctional electromagnetic interference shielding 3D reduced graphene oxide/vertical edge-rich graphene/

epoxy nanocomposites with remarkable thermal management performance, Compos. Sci. Technol. 222 (2022), https://doi.org/10.1016/j.compscitech.2022.109407.
[37] T.T.V. Tran, D.V.N. Vo, S.T. Nguyen, C.M. Vu, Silver nanowires decorated recycled cigarette filters based epoxy composites with high through-plane thermal conductivity and efficient electromagnetic interference shielding, Compos. Part A Appl. Sci. Manuf. 149 (2021), https://doi.org/10.1016/j.compositesa.2021.106485.
[38] Y. Yang, R. Bi, W. Ren, Y. Sun, H. Zhao, H. Duan, Oriented rGO framework induced hBN confined network in PDMS for absorption enhanced EMI shielding and through-plane thermal conductivity, Compos. Sci. Technol. 243 (2023), https://doi.org/10.1016/j.compscitech.2023.110259.
[39] Z. Shen, J. Feng, Preparation of thermally conductive polymer composites with good electromagnetic interference shielding efficiency based on natural wood-derived carbon scaffolds, ACS Sustain. Chem. Eng. 7 (2019) 6259–6266, https://doi.org/10.1021/acssuschemeng.8b06661.
[40] Y. Liu, M. Lu, K. Wu, S. Yao, X. Du, G. Chen, Q. Zhang, L. Liang, M. Lu, Anisotropic thermal conductivity and electromagnetic interference shielding of epoxy nanocomposites based on magnetic driving reduced graphene oxide@Fe 3 O 4, Compos. Sci. Technol. 174 (2019) 1–10, https://doi.org/10.1016/j.compscitech.2019.02.005.
[41] Y. Wang, L. Zhu, J. Wang, Y. Shangguan, Q. Zheng, Flexible, high thermal conductivity, and EMI shielding performance thermoplastic polyurethane composites through reinforced-orientation carbon fiber, ACS Appl. Polym. Mater. 6 (2024) 6057–6067, https://doi.org/10.1021/acsapm.4c00786.
[42] A.P. Singh, S. Tiwari, H. Sinhmar, G. Pal, A.K. Pandey, Experimental study on PCM (OM-37) enhanced with nanoparticles for improved heat retention in solar ponds, J. Energy Storage 123 (2025), https://doi.org/10.1016/j.est.2025.116760.
[43] .
[44] .
[45] .